

Article

Effect of Calcination Temperature on Structural Properties and Catalytic Performance of Novel Amorphous NiP/H β Catalyst for n-Hexane Isomerization

Jinshe Chen ^{1,*} , Lijun Zhu ², Yuzhi Xiang ² and Daohong Xia ^{2,*}

¹ College of Safety and Environmental Engineering, Shandong University of Science and Technology, Qingdao, Shandong 266590, China

² State Key Laboratory of Heavy Oil Processing, China University of Petroleum, Qingdao 266580, China; zhulj2002@163.com (L.Z.); xiangyzh@163.com (Y.X.)

* Correspondence: chenjins2010@163.com (J.C.); xiadh@upc.edu.cn (D.X.)

Received: 13 June 2020; Accepted: 15 July 2020; Published: 21 July 2020



Abstract: To study how calcination temperature influences the structural properties and catalytic performance of a novel amorphous NiP/H β catalyst, amorphous NiP/H β catalysts calcined at different temperatures were prepared for n-hexane isomerization. The optimum calcination temperature was determined, and the effect of calcination temperature on the structural properties of the catalysts was investigated using different characterization methods, such as XRD, TPD and so on. It was found that the optimum calcination temperature was 200 °C. Simultaneously, the amorphous NiP/H β catalyst showed good application potential as a non-noble metal catalyst. Calcination temperatures from 100 to 400 °C had almost no effect on pore properties. Meanwhile, the acid properties of the amorphous NiP/H β catalyst were affected very little by calcination temperature. By increasing calcination temperature, the dispersion state of amorphous NiP became worse at 300 °C, and then the structure of NiP changed from an amorphous structure into a crystalline structure at 400 °C. In addition, the catalyst became more difficult to reduce with the increase in calcination temperature. Combined with the results of n-hexane isomerization catalyzed by different samples, the mechanism by which calcination temperature affects n-hexane isomerization over catalyst was revealed. It was shown that for the amorphous NiP/H β catalyst, calcination temperature influences the catalytic performance mainly by affecting the dispersion degree and structure of active components.

Keywords: n-hexane isomerization; amorphous NiP/H β catalyst; calcination temperature; catalytic performance; influence mechanism

1. Introduction

In recent years, the isomerization of light alkanes has had an increasingly significant effect on improving the octane number of gasoline [1–5]. Due to the advantage of barely containing aromatics and olefins in its products, it is considered to be an environmentally friendly method in petroleum refining industry [6–9]. Recently, cleaner production has attracted more and more attention in various fields [10,11]. Now bifunctional metal/acid catalysts are extensively applied in the isomerization of light alkanes, and their active components are usually noble metals such as Pt and Pd [12–16]. Because of the existence of noble metals, the cost of catalysts is high, and their sulfur resistance is poor. Therefore, research into non-noble metal catalysts has attracted a lot of attention [17,18].

However, many current non-noble metal catalysts have low catalytic activity in the isomerization of n-alkanes compared with noble metal catalysts [17–19]. Fortunately, our recent study proved that

amorphous NiP/H β catalysts exhibit a good catalytic function in the isomerization of light alkanes. It is well known that calcination temperature is a vitally important factor for the catalyst. For different kinds of catalysts, calcination temperatures exhibit different degrees of influence on the dispersion state and structure of the active components, pore structures, as well as their acid properties and other properties [20–22]. Meanwhile, the change of structure and other properties of catalysts would lead to changes in catalytic activity [23,24], so it is significant to study the relationship between calcination temperatures and catalytic activity.

In consideration of the key questions mentioned above, a following research with respect to a novel amorphous NiP/H β catalyst was conducted in this paper, so as to systematically clarify the influence of calcination temperature on the structural properties of the catalyst and its catalytic performance with respect to isomerization of n-alkanes, which has not been reported before. The research could provide very important guidance for the development of new non-noble metal catalysts.

2. Materials and Methods

2.1. Catalyst Preparation

Nickel chloride (NiCl₂·6H₂O) and hypophosphorous acid (H₃PO₂) were used as reactants to synthesize amorphous NiP active components via chemical reduction; further details are provided the Support information [25,26].

The carrier was prepared via the mixture of H β molecular sieves and Al₂O₃. H β molecular sieves and Al₂O₃ were mixed as carrier according to a mass ratio of 3:1. A certain amount of amorphous NiP and carrier were fully mixed. After properly distilled water was added into the mixture, the products were extruded and dried at 70 °C for 2 h. Afterwards, products were continually calcined under N₂ at 100 °C, 200 °C, 300 °C and 400 °C, respectively. Finally, amorphous NiP/H β catalysts with different calcination temperatures were obtained.

2.2. Characterization Methods and Catalytic Activity Measurements

The analysis of the structures of different samples was performed by XRD. N₂ adsorption–desorption isotherms were analyzed by the Quantachrome Autosorb-1MP volumetric adsorption analyzer. The acid properties of the catalyst surfaces were measured using Py-IR and NH₃-TPD, respectively.

For Py-IR analysis, samples roasted at different temperatures were firstly kept at 100 °C for 2 h to remove water, and then they were exposed to gaseous pyridine at room temperature for 24 h under vacuum condition. After that, they were degassed for 2 h at 100 °C under vacuum condition to clear the pyridine of physical adsorption. Finally, the IR results were obtained at room temperature. For NH₃-TPD analysis, samples were heated from 50 °C to 100 °C, and after that, the samples were kept at 100 °C for 2 h under helium flow in order to remove water. Samples were saturated with ammonia after they had been cooled to 80 °C. Then they were purged by helium for 1 h, after which they were heated to 700 °C under helium flow (10 mL/min). The surface reduction properties of catalysts were characterized by H₂-TPR and the crystalline temperatures of the samples were studied by DSC. SEM-mapping and TEM were used to study the dispersion state. TEM was also used to analyze the diameters of active components. These methods were conducted as described in the Support information.

The n-hexane isomerization performance was evaluated using a fixed-bed reactor. The reaction tube was a 550 mm×8 mm stainless steel tube. Before the test, 4.0 g of the catalyst was placed in the middle of the reaction tube, and both ends of the catalyst were tightly filled with quartz sand. The evaluation method for the NiP/H β catalysts and the analysis method for the reaction products were performed as described in the Support information.

3. Results and Discussion

3.1. Characterization of Catalyst

Nitrogen adsorption isotherms for 10 wt% NiP/H β calcined at different temperatures are displayed in Figure 1, which show similar configurations and belong to the type I+IV isotherm. The hysteresis loops of all of the samples belong to the type H4, suggesting that narrow slit-like pores are contained in them. The fast adsorption of nitrogen in the isotherms is generated by the micropore structures of H β [27].

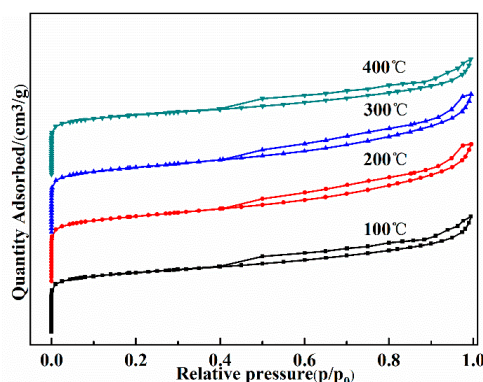


Figure 1. N₂ adsorption–desorption isotherms for 10 wt% NiP/H β calcined at different temperatures.

Figure 2 shows the size distribution curves of the samples. It can be observed that samples calcined at different temperatures have similar narrow pore size distributions. At the same time, there are two sharp pore distribution peaks, and their pore diameters are between 0.6 nm and 1.3 nm, respectively. The ranges of pore diameters are mainly from 0.5 nm to 0.7 nm, which is attributed to the microporous range.

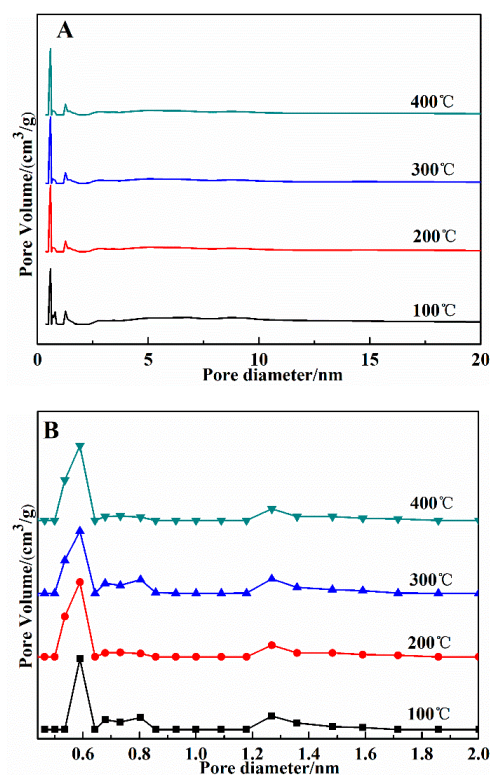


Figure 2. Pore size distribution curves for 10 wt% NiP/H β calcined at different temperatures. The range of pore diameter: (A) 0–35 nm and (B) 0–2 nm (magnification).

To better illustrate how calcination temperature further influences catalysts, the textural properties of different samples are listed in Table 1.

Table 1. Textural properties of 10 wt% NiP/H β calcined at different temperatures.

Calcination Temperatures/ $^{\circ}$ C	BET (m^2/g)	Vmp. ^a (cm^3/g)	V _T . ^b (cm^3/g)
100	412.09	0.14	0.30
200	411.10	0.14	0.30
300	412.11	0.14	0.31
400	411.29	0.13	0.30

^a Micropore volume as determined by t-plot and normalized per gram of support. ^b Total pore volume.

It could be clearly shown that the structural characteristics of samples remain almost the same when increasing roasting temperature. As shown by the above results (Figure 1, Figure 2 and Table 1), there is almost no change in the pore properties of catalysts when they are calcined from 100 to 400 $^{\circ}$ C, and the pore structure of catalysts exhibits good stability in this temperature range. The reason for this lies in the fact that both H β and Al₂O₃ of the carrier have good thermal stability, and the pore structures of the samples remained intact below 400 $^{\circ}$ C.

The XRD results of the samples calcined from 100 to 400 $^{\circ}$ C are presented in Figure 3. For samples prepared at temperatures below 300 $^{\circ}$ C, only diffraction signals of H β and Al₂O₃ could be observed in the catalysts [28], which could be ascribed to the fact that the NiP loadings of samples were relatively low, and in the meantime, the NiP nanoparticles of the samples at temperatures below 300 $^{\circ}$ C retained their amorphous structure. When the roasting temperature of NiP/H β was further increased to 400 $^{\circ}$ C, the XRD pattern of the sample began to obviously change. It can be seen that obvious peaks other than the peaks of carrier begin to appear at 2θ values of 44.6 $^{\circ}$ and 51.9 $^{\circ}$, implying the formation of more stable crystalline Ni on the catalyst surface at high temperature [29,30].

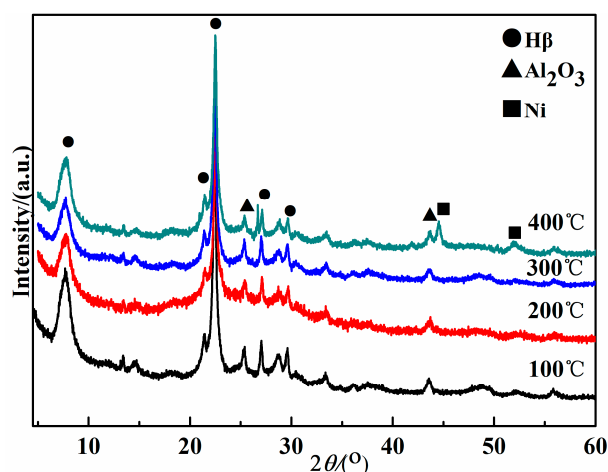


Figure 3. XRD patterns of NiP/H β calcined at different temperatures.

Figure 4 shows the DSC results of the NiP nanoparticles when determining the crystalline temperature. There is an obvious endothermic peak below 200 $^{\circ}$ C, which is mainly caused by the release of adsorbed water. As the heating temperature increases, two exothermic peaks located at about 360 and 460 $^{\circ}$ C can be observed, which are related to the crystallization of amorphous NiP nanoparticles. The exothermic peak at 360 $^{\circ}$ C can probably be ascribed to the structural transformation of NiP active components from amorphous phase into crystalline Ni₃P [31]. The exothermic peak at about 460 $^{\circ}$ C is probably related to the transformation of metastable phase to stable Ni phase, a process that begins at about 440 $^{\circ}$ C.

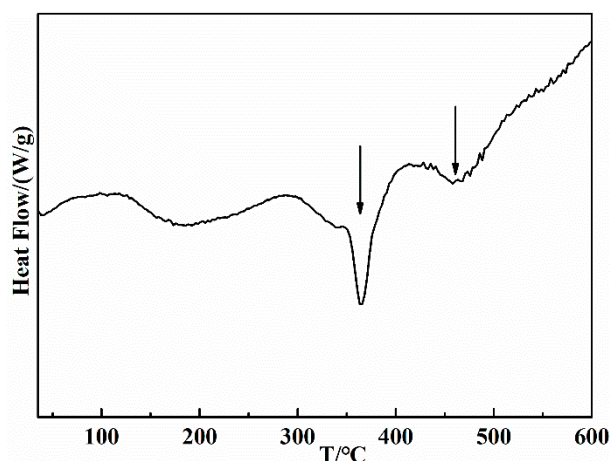


Figure 4. DSC curve of NiP.

As can be seen from Figure 5A, the TEM micrographs of amorphous NiP/H β calcined at 200 °C show that NiP nanoparticles have spherical or chainlike structures, with average diameters ranging from 50 to 100 nm. For NiP/H β calcined at 200 °C, NiP nanoparticles supported on carrier show good dispersion. When the calcination temperature was 300 °C, there were no obvious changes in the average diameters and shapes of NiP nanoparticles (Figure 5B), implying that the active components still retain a good amorphous structure. However, compared with samples calcined at temperatures below 200 °C, the degree of dispersion of active components becomes worse when the temperature reaches 300 °C. With the increase in calcination temperature to 400 °C (Figure 5C), the sizes of the NiP nanoparticles decreased rapidly, and the state of active components changes into a crystalline state. Owing to the decrease in the size of the NiP nanoparticles after crystallization, the degree of dispersion of the NiP nanoparticles improves instead. Moreover, the SAED picture of NiP/H β calcined at 400 °C is displayed in Figure 5D to further determine the structure of active components. Figure 5D shows that some bright white spots exist in the SAED picture, sufficiently confirming that the structure of the NiP active components has partly changed from an amorphous state into a crystalline state. The TEM results are basically confirmed by the XRD and DSC results.

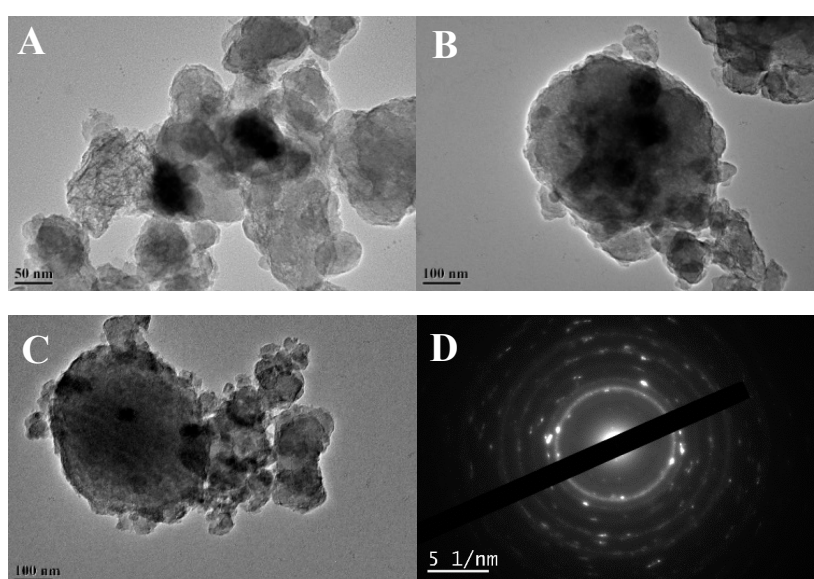


Figure 5. TEM micrographs of the samples: (A) NiP/H β calcined at 200 °C, (B) NiP/H β calcined at 300 °C, (C) NiP/H β calcined at 400 °C and (D) SAED picture of NiP/H β calcined at 400 °C.

Figure 6 shows the SEM-mappings of the catalyst, containing the dispersion of P and Ni, respectively. For the catalyst calcined at 200 °C, the amorphous NiP nanoparticles are dispersed well, and the results are coincident with the XRD (Figure 3) and TEM results (Figure 5).

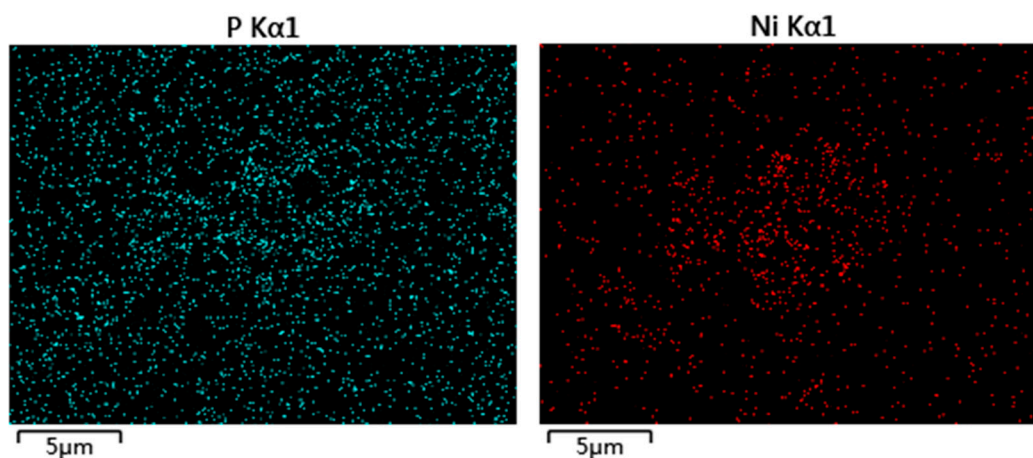


Figure 6. SEM-mappings of NiP/H β calcined at 200 °C.

Absorbance peaks characteristic of hydrogen-bound pyridine (H), Brønsted (B), weak Lewis (WL), and strong Lewis (SL) sites are indicated.

The Py-IR spectra of catalysts roasted at different temperatures are shown in Figure 7. The bands generated by pyridine adsorbed on Brønsted (B) and Lewis (L) acid sites are located at approximately 1540 and 1450 cm^{-1} , respectively. On the whole, there is almost no difference in the number of Brønsted and Lewis acid sites for samples roasted at different temperatures [32,33]. The bands appearing at around 1610 and 1575 cm^{-1} suggest the existence of strong and weak Lewis acid sites, respectively [34]. The numbers of strong Lewis (SL) acid sites in samples calcined at 100 °C, 200 °C and 300 °C are almost the same [35]; however, the number of SL acid sites in the sample roasted at 400 °C is slightly decreased in comparison with the other samples. The reason for this can be attributed to the fact that the existence of SL acid sites is closely associated with the unsaturated nickel atoms of amorphous NiP nanoparticles. When the calcination temperature is increased to 400 °C, NiP nanoparticles gradually transform from their amorphous state into a crystalline Ni phase (Figure 3), decreasing the amount of unsaturated Ni atoms and ultimately leading to a decrease in the number of SL acid sites.

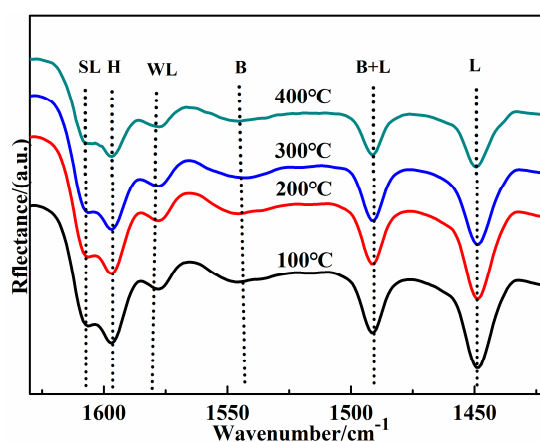


Figure 7. Py-IR spectra of 10 wt% NiP/H β calcined at different temperatures.

The NH₃-TPD profiles of samples calcined at different temperatures are displayed in Figure 8. It can be seen that there is almost no difference in the NH₃-TPD patterns for the different samples.

In the range of 80–650 °C, a broad desorption curve with a desorption peak at about 170 °C appears for all samples, and another desorption peak appears at about 390 °C, suggesting that there are two types of acid site existing on the sample surfaces.

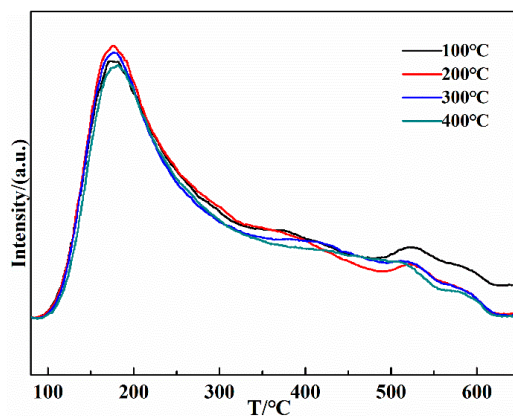


Figure 8. NH₃-TPD profiles of 10 wt% NiP/H β calcined at different temperatures.

The desorption peak curves below 300 °C are closely related with the weak acid sites, and those above 300 °C imply that there are also SL sites on the catalysts [36,37]. Nevertheless, the peak located at about 500 °C becomes very weak for the sample calcined at a temperature of 400 °C, due to the fact that the number of unsaturated Ni atoms decreases as the decomposition of most of the amorphous NiP nanoparticles into stable Ni (Figures 3 and 4) [38]. It can be observed that the NH₃-TPD results are consistent with the results of Py-IR spectra (Figure 7), indicating that when the calcination temperature was 400 °C, the decrease of strong acid sites was mainly strong Lewis sites. Overall, the above results reveal that the acid properties of amorphous NiP/H β catalysts were minimally affected by calcination temperature, having good stability at temperatures ranging from 100 °C to 400 °C.

The reduction profiles of different samples are presented in Figure 9. Two distinct reduction peaks can be observed in the TPR curves of all of the samples, implying that there are two reducible species appearing in the reduction process under the H₂ atmosphere. The low-temperature peak is probably generated by the reduction of the amorphous NiP nanoparticles into Ni₃P; meanwhile, the high-temperature peak can be attributed to the reduction of Ni₃P into Ni on the catalyst [31,39]. With the increase in calcination temperature for samples from 100 °C to 400 °C, the low-temperature reduction peak gradually increases from 330 °C to 400 °C, and the high-temperature peak gradually increases from 450 °C to 600 °C. It can be observed that catalysts are more difficult to reduce with the increase in calcination temperature, and the increased difficulty in reduction could be related to the stronger interaction of NiP nanoparticles and Ni₃P reducible species with the carrier.

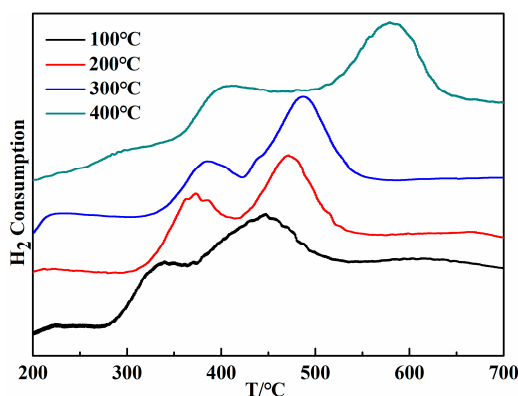


Figure 9. The TPR profiles of 10 wt% NiP/H β calcined at different temperatures.

3.2. Catalytic Activity and Influence Mechanism

Reaction conditions: $T = 290\text{ }^{\circ}\text{C}$, $P = 2.0\text{ MPa}$, $\text{WHSV} = 1.0\text{ h}^{-1}$, H_2 -to-n-hexane molar ratio = 4.0, Reaction time = 4 h.

The effect of calcination temperatures on n-hexane isomerization is displayed in Figure 10, showing the n-hexane conversion and the yield of isomerization products, respectively. To reduce the experimental errors of catalytic testing, the data were all tested three times, and then averaged.

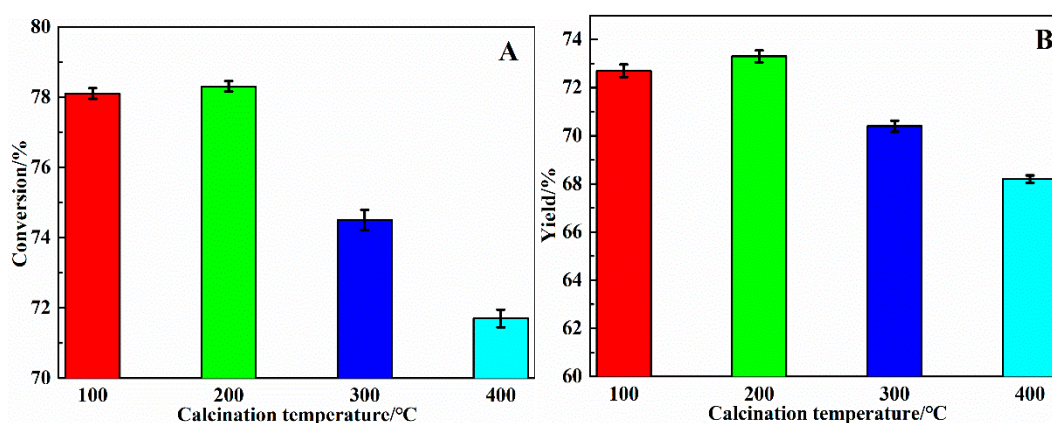


Figure 10. Effect of calcination temperatures on (A) the n-hexane conversion, and (B) the yield of iso-alkanes ($i\text{-C}_5$ and $i\text{-C}_6$).

The results show that n-hexane conversion and yield of isomerization products have the same variation tendency, and that they first increase and then subsequently decrease with increasing calcination temperatures of the samples. When calcination temperatures were increased to $200\text{ }^{\circ}\text{C}$, both the n-hexane conversion and yield of isomerization products simultaneously reached their maximum. The catalytic performance of the sample calcined at $100\text{ }^{\circ}\text{C}$ was slightly reduced in comparison with the sample calcined at $200\text{ }^{\circ}\text{C}$.

To further confirm the effect of calcination temperatures on catalytic activity, the product distributions of 10 wt% NiP/H β calcined at different temperatures are listed in Table 2. As shown in Table 2, both the n-hexane conversion and yield of iso-alkanes ($i\text{-C}_6$ and $i\text{-C}_{5,6}$) first increase and then decrease with the increase in calcination temperature from $100\text{ }^{\circ}\text{C}$ to $400\text{ }^{\circ}\text{C}$. The catalyst calcined at $200\text{ }^{\circ}\text{C}$ has the best catalytic activity. Especially with respect to the high-octane components 2,2-dimethyl butane and 2,3-dimethyl butane, their yield reached up to 18.2% when the temperature is $200\text{ }^{\circ}\text{C}$. Meanwhile, for crystalline Ni/SAPO-11 catalyst, the n-hexane conversion was about 73% and the yield of high-octane components 2,2-dimethyl butane and 2,3-dimethyl butane was about 5% [40]. Additionally, for noble metal Pt/HY catalyst, the n-hexane conversion was about 74%, and the yield of high-octane components 2,2-dimethyl butane and 2,3-dimethyl butane was less than 17% [41]. The comparison results convincingly imply that the amorphous NiP/H β catalyst has good application prospects.

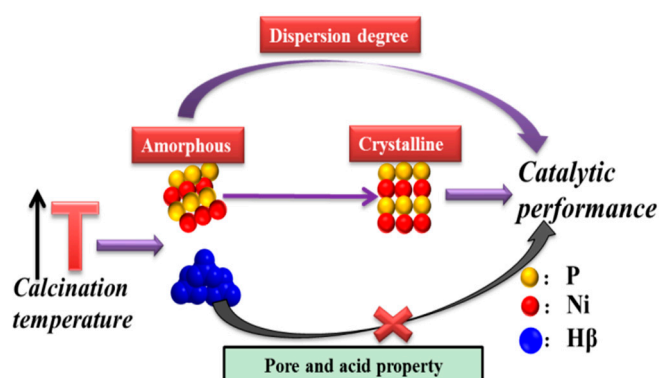
Table 2. The product distribution of 10 wt% NiP/H β calcined at different temperatures.

Components	Wt. % of n-Hexane Converted to Different Components			
	100 °C	200 °C	300 °C	400 °C
<C ₄	1.0	0.9	0.8	0.7
iC ₄	0.7	0.6	0.5	0.3
nC ₄	1.8	1.7	1.3	1.1
iC ₅	2.5	1.5	0.9	0.3
nC ₅	1.9	1.8	1.5	1.4
2,2-dimethyl butane	8.1	10.1	6.3	4.7
2,3-dimethyl butane	8.2	8.1	8.4	8.5
2- methyl pentane	32.2	31.5	32.2	32.3
3- methyl pentane	21.7	22.1	22.6	22.4
i-C ₆	70.2	71.8	69.5	67.9
i-C ₅₋₆	72.7	73.3	70.4	68.2
nC ₆	21.9	21.7	25.5	28.3
Conversion	78.1	78.3	74.5	71.7

Reaction conditions: T = 290 °C, P = 2.0 MPa, WHSV = 1.0 h⁻¹, H₂-to-n-hexane molar ratio = 4.0, Reaction time = 4 h.

The results for Py-IR (Figure 7) and NH₃-TPD (Figure 8) reveal that calcination temperature has no significant impact on acid properties. At the same time, the results for the textural properties of the samples (Table 1) show that calcination temperature has almost no influence on pore properties. Combined with the results of n-hexane isomerization for samples with different calcination temperatures (Figure 10), the conclusion could be drawn that the difference in catalytic performance is not caused by the changes in acid properties and pore properties for amorphous NiP/H β catalyst. With respect to NiP nanoparticles as the active components of alkane isomerization catalysts for hydrogenation and dehydrogenation, their dispersion state and structure in the catalyst have a significant influence on their catalytic performance. As can be seen from Figures 3 and 5, for the catalysts calcined at 100 °C and 200 °C, the NiP nanoparticles could maintain their amorphous state and their dispersion properties were good. At the same time, their catalytic activities were good, and were nearly the same. By increasing calcination temperature from 200 °C to 300 °C, although NiP nanoparticles maintained their amorphous state, the degree of dispersion decreased slightly (Figure 5). These result suggest that the reduction of the reactivity for the sample calcined at 300 °C was probably due to the decreased dispersion properties of the active components. When the calcination temperature was increased to 400 °C, crystalline Ni began to be observed on the sample surface (Figure 3) and the catalytic activity continued to decrease (Figure 10).

Based on the results described above, the mechanism by which calcination temperature influences the amorphous NiP/H β catalyst is studied and proposed (Scheme 1). In the process of the catalytic reaction, NiP nanoparticles act as hydrogenation–dehydrogenation centers. H β zeolites act as acid centers and provide the reaction space. For the amorphous NiP/H β catalyst, calcination temperature has no significant impact on pore properties and acid properties, indicating that the acid and pore properties are not key factors that result in changes of catalytic activity. However, calcination temperature could significantly affect the dispersion state and structure of active components, which may first transform from amorphous NiP into crystalline Ni₃P and then further convert into stable crystalline Ni. In the process of increasing the calcination temperature, their dispersion degree first became worse, leading to a decrease in the uniformity of the metal sites. In addition, the state of the active components then transformed from an amorphous structure into a crystalline structure, leading to a decrease of the disorder degree of the active components. Based on the above reasons, the catalytic performance of n-hexane isomerization is ultimately influenced.



Scheme 1. Mechanism of the effect of calcination temperature on catalytic performance for amorphous NiP/H β catalyst.

The stability of catalysts is an important aspect for application, and their long-reaction activity was studied. The results are shown in Figure S1 (Support information). It can be clearly seen that n-C₆ conversion remains above 75% after 3 h, with selectivity to isomers (C₅–C₆) of above 90% and yield of isomers above 72%. The catalyst could maintain good catalytic stability for at least 300 h, implying that it has good catalytic stability.

4. Conclusions

For the amorphous NiP/H β catalyst, calcination temperatures from 100 to 400 °C have almost no effect on pore properties, due to the fact that H β and Al₂O₃ have good thermal stability in carrier. Meanwhile, the acid properties of amorphous NiP/H β catalysts were minimally affected by calcination temperature, exhibiting good stability in the temperature range from 100 °C to 400 °C. However, the amount of SL acid sites on the sample calcined at 400 °C was slightly reduced compared with the other samples, on account of the reduction of amorphous NiP nanoparticles. Moreover, by increasing the roasting temperature, catalysts were more difficult to reduce. As calcination temperature increases, the dispersion state of the amorphous NiP becomes worse at 300 °C, while the structure of the amorphous NiP as an active component subsequently gradually changes into crystalline Ni₃P and Ni. As calcination temperature increases, the catalytic activity of the samples first increased, and then decreased. When calcination temperature was 200 °C, the yield of the high-octane components 2,2-dimethyl butane and 2,3-dimethyl butane reached up to 18.2%.

Combined with the catalytic activity of n-hexane isomerization catalyzed by different samples, the influence mechanism is revealed. For amorphous NiP/H β catalyst, calcination temperature influences the catalytic activity of n-hexane isomerization mainly by affecting the dispersion state and the structure of the active components.

Supplementary Materials: The following are available online at <http://www.mdpi.com/2073-4344/10/7/811/s1>.

Author Contributions: Conceptualization, J.C. and D.X.; methodology, J.C.; validation, J.C., D.X.; formal analysis, L.Z., Y.X.; resources, J.C.; data curation, J.C.; writing—original draft preparation, J.C.; writing—review and editing, J.C.; supervision, J.C. and D.X.; project administration, J.C.; funding acquisition, J.C., L.Z. and D.X. All authors have read and agreed to the published version of the manuscript.

Funding: This research was funded by the National Natural Science Foundation of China (Grant U1662115) and Shandong Province Natural Science Foundation (ZR2019MB057).

Conflicts of Interest: The authors declare no conflict of interest.

References

1. Setiabudi, H.D.; Jalil, A.A.; Triwahyono, S.; Kamarudin, N.H.N.; Jusoh, R. Ir/Pt-HZSM5 for n-pentane isomerization: Effect of Si/Al ratio and reaction optimization by response surface methodology. *Chem. Eng. J.* **2013**, *217*, 300–309. [[CrossRef](#)]
2. Chica, A.; Corma, A. Hydroisomerization of Pentane, Hexane, and Heptane for improving the Octane Number of Gasoline. *J. Catal.* **1999**, *187*, 167–176. [[CrossRef](#)]
3. Arribas, M.A.; Márquez, F.; Martínez, A. Activity, Selectivity, and Sulfur Resistance of Pt/WO_x-ZrO₂ and Pt/Beta Catalysts for the Simultaneous Hydroisomerization of n-Heptane and Hydrogenation of Benzene. *J. Catal.* **2000**, *190*, 309–319. [[CrossRef](#)]
4. Tamizhdurai, P.; Ramesh, A.; Santhana Krishnan, P.; Narayanan, S.; Shanthi, K.; Sivasanker, S. Effect of acidity and porosity changes of dealuminated mordenite on n-pentane, n-hexane and light naphtha isomerization. *Microporous Mesoporous Mater.* **2019**, *287*, 192–202. [[CrossRef](#)]
5. Yang, L.; Wang, W.; Song, X.M.; Bai, X.F.; Feng, Z.L.; Liu, T.; Wu, W. The hydroisomerization of n-decane over Pd/SAPO-11 bifunctional catalysts: The effects of templates on characteristics and catalytic performances. *Fuel Process. Technol.* **2019**, *190*, 13–20. [[CrossRef](#)]
6. Setiabudi, H.D.; Jalil, A.A.; Triwahyono, S. Ir/Pt-HZSM5 for n-pentane isomerization: Effect of iridium loading on the properties and catalytic activity. *J. Catal.* **2012**, *294*, 128–135. [[CrossRef](#)]
7. Zhang, R.; Meng, X.H.; Liu, Z.C.; Meng, J.Y.; Xu, C.M. Isomerization of n-Pentane Catalyzed by Acidic Chloroaluminate Ionic Liquids. *Ind. Eng. Chem. Res.* **2008**, *47*, 8205–8210. [[CrossRef](#)]
8. Gao, L.; Shi, Z.Y.; Jerome Etim, U.; Wu, P.P.; Xing, W.; Zhang, Y.; Bai, P.; Yan, Z.F. Superior catalytic performance of micro-mesoporous Beta-SBA-15 composite with a high indexed isomerization factor in hydroisomerization of n-heptane. *Fuel* **2019**, *252*, 653–665. [[CrossRef](#)]
9. Rizescu, C.; Cojocaru, B.; Thanh Hien, N.T.; Huyenb, P.T.; Parvulescu, V.I. Synergistic B-Al interaction in SBA-15 affording an enhanced activity for the hydro-isomerization of heptane over PteBeAl-SBA-15 catalysts. *Microporous Mesoporous Mater.* **2019**, *281*, 142–147. [[CrossRef](#)]
10. Bao, Q.; Nie, W.; Liu, C.Q.; Zhang, H.H.; Wang, H.K.; Jin, H.; Yan, J.Y.; Liu, Q. The preparation of a novel hydrogel based on crosslinked polymers for suppressing coal dusts. *J. Clean. Prod.* **2020**, *249*, 1–12. [[CrossRef](#)]
11. Yuan, M.Y.; Nie, W.; Zhou, W.W.; Yan, J.Y.; Bao, Q.; Guo, C.J.; Tong, P.; Zhang, H.H.; Guo, L.D. Determining the effect of the non-ionic surfactant AEO9 on lignite adsorption and wetting via molecular dynamics (MD) simulation and experiment comparisons. *Fuel* **2020**, *278*, 1–13. [[CrossRef](#)]
12. Roldán, R.; Beale, A.M.; Sánchez-Sánchez, M.; Romero-Salguero, F.J.; Jiménez-Sanchidrián, C.; Gómez, J.P.; Sankar, G. Effect of the impregnation order on the nature of metal particles of bi-functional Pt/Pd-supported zeolite beta materials and on their catalytic activity for the hydroisomerization of alkanes. *J. Catal.* **2008**, *254*, 12–26.
13. Li, H.; Li, M.; Chu, Y.; Nie, H. Influence of different modified zeolite on skeletal isomerization of n-hexene in the presence of hydrogen. *Microporous Mesoporous Mater.* **2009**, *117*, 635–639. [[CrossRef](#)]
14. Santiesteban, J.G.; Calabro, D.C.; Chang, C.D.; Vartuli, J.C.; Fiebig, T.J.; Bastian, R.D. The role of platinum in hexane isomerization over Pt/FeO_y/WO_x/ZrO₂. *J. Catal.* **2001**, *202*, 25–33. [[CrossRef](#)]
15. Duchet, J.C.; Guillaume, D.; Monnier, A.; Dujardin, C.; Gilson, J.P.; Gestel, J.V.; Szabo, G.; Nascimento, P. Isomerization of n-hexane over sulfated zirconia: Influence of hydrogen and platinum. *J. Catal.* **2001**, *198*, 328–337. [[CrossRef](#)]
16. Triwahyono, S.; Jalil, A.A.; Izan, S.M.; Jamari, N.S.; Fatah, A.A. Isomerization of linear C₅-C₇ over Pt loaded on protonated fibrous silica@Y zeolite (Pt/HSi@Y). *J. Energy Chem.* **2019**, *37*, 163–171. [[CrossRef](#)]
17. Masalska, A.; Grzechowiak, J.R.; Jaroszevska, K. Effect of metal-support interactions in Ni/ZSM-5 + Al₂O₃ catalysts on the transformation of n-paraffins. *Top. Catal.* **2013**, *56*, 981–994. [[CrossRef](#)]
18. Ohno, T.; Li, Z.; Sakai, N.; Sakagami, H.; Takahashi, N.; Matsuda, T. Heptane isomerization over molybdenum oxides obtained by H₂ reduction of H_xMoO₃ with different hydrogen contents. *Appl. Catal. A Gen.* **2010**, *389*, 52–59. [[CrossRef](#)]
19. Goguet, A.; Shekhtman, S.; Cavallaro, F.; Hardacre, C.; Meunier, F.C. Effect of the carburization of MoO₃-based catalysts on the activity for butane hydroisomerization. *Appl. Catal. A Gen.* **2018**, *344*, 30–35. [[CrossRef](#)]

20. Belandria, L.; Marín-Astorg, N.; García, E.; Sos, E.; Aguirre, F.; Villarroel, M.; Uzcátegui, A. Catalytic activity of Pt and Pd catalysts supported on HWP/HMS in the selective hydroisomerization of n-pentane. Effect of reaction temperature. *Catal. Today* **2011**, *172*, 2–7. [[CrossRef](#)]
21. Song, Y.Q.; Tian, J.; Ye, Y.R.; Jin, Y.Q.; Zhou, X.L.; Wang, J.; Xu, L.Y. Effects of calcination temperature and water-washing treatment on n-hexane hydroisomerization behavior of Pt-promoted sulfated zirconia based catalysts. *Catal. Today* **2013**, *212*, 108–114. [[CrossRef](#)]
22. Zhou, X.L.; Yu, G.X.; Tang, C.; Li, C.L.; Wang, J.A.; Novaro, O.; Llanos, M.E.; Cortés-Jácome, M.A. On the Role of Calcination Temperature in Pt-SO₄²⁻/ZrO₂-Al₂O₃ Preparation and Catalytic Behaviors During the n-Hexane Hydroisomerization. *Catal. Lett.* **2008**, *124*, 277–283. [[CrossRef](#)]
23. Zhang, M.; Chen, L.M.; Yao, S.Y.; Long, Y.M.; Li, W.F.; Wang, Z.S. Effect of calcination temperature on the photocatalytic activity of CaSb₂O₆ nanoparticles prepared by co-precipitation method. *Catal. Commun.* **2014**, *48*, 29–32. [[CrossRef](#)]
24. Wang, G.W.; Wu, W.L.; Zhu, X.L.; Sun, Y.N.; Li, C.Y.; Shan, H.H. Effect of calcination temperature on isobutane dehydrogenation over Mo/MgAl₂O₄ catalysts. *Catal. Commun.* **2014**, *56*, 119–122. [[CrossRef](#)]
25. Ma, Y.F.; Zhang, M.H.; Li, W.; Zhang, B.G.; Tao, K.Y. Preparation and catalytic activity of NiP amorphous alloy with high surface area. *Chin. J. Catal.* **2004**, *25*, 973–978.
26. Ma, Y.F.; Li, W.; Zhang, M.H.; Zhang, B.G.; Tao, K.Y. New method of preparing NiP and NiPB amorphous alloys using nickel hypophosphite as reactant. *Acta Phys.-Chim. Sin.* **2002**, *18*, 938–942.
27. Deng, H.X.; Grunder, S.; Cordova, K.E.; Valente, C.; Furukawa, H.; Hmadeh, M.; Gándara, F.; Whalley, A.C. Large-pore apertures in a series of metal-organic frameworks. *Science* **2012**, *336*, 1018–1023. [[CrossRef](#)] [[PubMed](#)]
28. Wan, G.F.; Duan, A.J.; Zhang, Y.; Zhao, Z.; Jiang, G.Y.; Zhang, D.Q.; Gao, Z.Y.; Liu, J. Hydrodesulfurization of Fluidized Catalytic Cracking Diesel Oil over NiW/AMB Catalysts Containing H-Type β-Zeolite in Situ Synthesized from Kaolin Material. *Energy Fuels* **2019**, *23*, 3846–3852. [[CrossRef](#)]
29. Kapfenberger, C.; Hofmann, K.; Albert, B. Room-temperature synthesis of metal borides. *Solid State Sci.* **2003**, *5*, 925–930. [[CrossRef](#)]
30. Wang, M.; Li, H.; Wu, Y.; Zhang, J. Comparative studies on the catalytic behaviors between the Ni-B amorphous alloy and other Ni-based catalysts during liquid phase hydrogenation of acetonitrile to ethylamine. *Mater. Lett.* **2003**, *57*, 2954–2964. [[CrossRef](#)]
31. Zhao, Y.; Zhao, Y.P.; Feng, H.G.; Shen, J.Y. Synthesis of nickel phosphide nano-particles in a eutectic mixture for hydrotreating reactions. *J. Mater. Chem.* **2011**, *21*, 8137–8145. [[CrossRef](#)]
32. Guo, L.; Bao, X.J.; Fan, Y.; Shi, G.; Liu, H.Y.; Bai, D.J. Impact of cationic surfactant chain length during SAPO-11 molecular sieve synthesis on structure, acidity, and n-octane isomerization to di-methyl hexanes. *J. Catal.* **2012**, *294*, 161–170. [[CrossRef](#)]
33. Chen, L.F.; Zhou, X.L.; Noreña, L.E.; Wang, J.A.; Navarrete, J.; Salas, P.; Montoya, A.; Angel, P.D.; Llanos, M.E. Comparative studies of Zr-based MCM-41 and MCM-48 mesoporous molecular sieves: Synthesis and physicochemical properties. *Appl. Surf. Sci.* **2006**, *253*, 2443–2451. [[CrossRef](#)]
34. Gu, Y.; Liu, S.; Li, C.; Cui, Q. Selective conversion of glycerol to acrolein over supported nickel sulfate catalysts. *J. Catal.* **2013**, *301*, 93–102. [[CrossRef](#)]
35. Chakraborty, B.; Viswanathan, B. Surface acidity of MCM-41 by in situ IR studies of pyridine adsorption. *Catal. Today* **1999**, *49*, 253–260. [[CrossRef](#)]
36. Kim, Y.T.; Jung, K.D.; Park, E.D. Gas-phase dehydration of glycerol over ZSM-5 catalysts. *Micropor. Mesoporous Mater.* **2010**, *131*, 28–36. [[CrossRef](#)]
37. Cai, C.; Wang, H.; Han, J. Synthesis and characterization of ionic liquid-functionalized alumino-silicate MCM-41 hybrid mesoporous materials. *Appl. Surf. Sci.* **2011**, *257*, 9802–9808. [[CrossRef](#)]
38. Cecilia, J.A.; Jiménez-Morales, I.; Infantes-Molina, A.; Rodríguez-Castellón, E.; Jiménez-López, A. Influence of the silica support on the activity of Ni and Ni₂P based catalysts in the hydrodechlorination of chlorobenzene. Study of factors governing catalyst deactivation. *J. Mol. Catal. A Chem.* **2013**, *368–369*, 78–87. [[CrossRef](#)]
39. Chen, J.X.; Ci, D.H.; Wang, R.J.; Zhang, J.Y. Hydrodechlorination of chlorobenzene over NiB/SiO₂ and NiP/SiO₂ amorphous catalysts after being partially crystallized: A consideration of electronic and geometrical factors. *Appl. Surf. Sci.* **2008**, *255*, 3300–3309. [[CrossRef](#)]

40. Lyu, Y.C.; Yu, Z.M.; Yang, Y.; Wang, X.H.; Zhao, X.X.; Liu, X.M.; Yan, Z.F. Metal-acid balance in the in-situ solid synthesized Ni/SAPO-11 catalyst for n-hexane hydroisomerization. *Fuel* **2019**, *243*, 398–405. [[CrossRef](#)]
41. Boskovic, G.; Micic, R.; Pavlovic, P.; Putanov, P. n-Hexane isomerization over Pt–Na(H)Y catalysts obtained by different preparation methods. *Catal. Today* **2001**, *65*, 123–128. [[CrossRef](#)]



© 2020 by the authors. Licensee MDPI, Basel, Switzerland. This article is an open access article distributed under the terms and conditions of the Creative Commons Attribution (CC BY) license (<http://creativecommons.org/licenses/by/4.0/>).